

Stable Formamidinium-Based Centimeter Long Two-Dimensional Lead Halide Perovskite Single-Crystal for Long-Live Optoelectronic Applications

Rajesh Kumar Ulaganathan,* Raghavan Chinnambedu Murugesan,* Chang-Yu Lin, Ambika Subramanian, Wei-Liang Chen, Yu-Ming Chang, Alex Rozhin, and Raman Sankar*

Solution-processable 2D metal-halide perovskites are highly promising for cost-effective optoelectronic applications due to their intrinsic multiquantum well structure. However, the lack of stability is still a major obstacle in the use of this class of materials in practical devices. Here, the authors demonstrate the stable optoelectronic properties using formamidinium (FA)-based centimeter-long 2D perovskite $(\text{BA})_2\text{FAPb}_2\text{I}_7$ high-quality single-crystal controlled by the thickness of two perovskite layers. The large area single-crystal exhibits good crystallinity, phase purity, and spectral uniformity. Moreover, the $(\text{BA})_2\text{FAPb}_2\text{I}_7$ single-crystal shows excellent stability at open atmospheric conditions when compared to methylammonium (MA)-based $(\text{BA})_2\text{MAPb}_2\text{I}_7$ counterparts. The photodetectors fabricated using 2D perovskite single-crystal on the rigid Si/SiO₂ substrate reveal high photoresponsivity (R_λ) ($\approx 5 \text{ A W}^{-1}$), the fast response time ($< 20 \text{ ms}$), specific detectivity (D^*) ($\approx 3.5 \times 10^{11}$ Jones), and excellent durability under 488 nm laser illumination. The R_λ and D^* values are obtained from the $(\text{BA})_2\text{FAPb}_2\text{I}_7$ single-crystal 25 times and three orders magnitudes, respectively, higher than the $(\text{BA})_2\text{MAPb}_2\text{I}_7$ single-crystal. Additionally, the perovskite material on flexible polymer substrate reveals good photo-sensing properties in both bending and nonbending states.

light-emitting diode (LED),^[8] and laser^[9] applications. However, chemical degradation due to poor ambient stability limits their use in practical applications. Ruddlesden–Popper (RP) 2D-MHPs represented by the generic formula $(\text{A}')_2\text{A}_{n-1}\text{M}_n\text{X}_{3n+1}$, where A' is a long-chain organic spacer, such as butyl ammonium (BA) cation ($\text{C}_4\text{H}_9\text{NH}_3^+$), “A” is small organic methylammonium (MA) cation (CH_3NH_3^+), M is divalent metal ions (Pb^{2+}), X is halide ions (Cl^- , Br^- , and I^-), and “n” are integers ($n = 1, 2, 3, 4, \dots$), drew much attention due to quantum confinement and better stability.^[10–13]

The 2D-MHP forms a self-assembled multiquantum well structure through the alternative stacking of MHP and long-chain organic spacers in the RP phase.^[10] The semiconducting perovskite slabs act as potential “wells,” and the insulating cationic long-chain organic spacers act as potential “barrier” layers. The number of conductive slabs per unit cell determines quantum well thickness.^[10] Due to quantum confinement, 2D-MHPs exhibits stable exciton emission, high exciton binding energy, quantum yield, high carrier mobility, anisotropy, and tunable optoelectronic properties.^[10] Among existed 2D-MHPs, homologous $(\text{BA})_2(\text{MA})_{n-1}\text{Pb}_n\text{X}_{3n+1}$ with the range of “n” values were widely explored in the form of large-area thin films and bulk single-crystals for solar cells,^[13,14] photodetector,^[15] LEDs,^[16,17] optical pumping,^[18,19] and transistor^[20] applications.

1. Introduction

ABX_3 ($\text{A} = \text{CHNH}_3^+$, $\text{B} = \text{Pb}$, and $\text{X} = \text{Cl}$, Br , and I) metal-halide perovskites (MHPs) are currently being well explored due to outstanding solar cell performance with power conversion efficiency greater than 25% by solution process.^[1] High optical absorption coefficient,^[2] low binding energy,^[3] long carrier diffusion,^[4] and tunable band gap^[5] make this class of materials promising in photodetector,^[6] solar cell,^[7]

R. K. Ulaganathan
Department of Photonics Engineering
Technical University of Denmark
Lyngby 2800, Denmark
E-mail: rajul@fotonik.dtu.dk

R. K. Ulaganathan, W.-L. Chen, Y.-M. Chang
Center for Condensed Matter Sciences
National Taiwan University
Taipei 10617, Taiwan

 The ORCID identification number(s) for the author(s) of this article can be found under <https://doi.org/10.1002/adfm.202112277>.

DOI: 10.1002/adfm.202112277

R. K. Ulaganathan, R. Sankar
Institute of Physics
Academia Sinica
Taipei 11529, Taiwan
E-mail: sankarraman@gate.sinica.edu.tw

R. C. Murugesan, A. Rozhin
Aston Institute of Photonic Technologies
Aston University
Birmingham B4 7ET, UK
E-mail: chinnamr@aston.ac.uk

C.-Y. Lin, A. Subramanian
Department of Mechanical Engineering
Chung Yuan Christian University
Taoyuan 32023, Taiwan

Although the 2D perovskites exhibit relatively better stability than their 3D counterparts,^[10] atmospheric degradation persists as a severe problem in niching them into proper applications. Particularly, the perovskite architecture formed by the MA cation undergoes easy degradation in the ambient atmosphere due to structural instability caused by the low tolerance factor.^[21,22] Replacement of smaller ionic radius MA cation (≈ 2.17 Å) with larger formamidinium (FA) cation (≈ 2.53 Å) was proved to potentially stabilize the crystal structure by sustaining the tolerance requirements which in turn enhanced the atmospheric and thermal degradation of the MHPs.^[22,23] However, applications of FA-based MHPs are mostly limited to 3D FAPbX₃ perovskites.^[23–25] The systematic study on degradation stability and optoelectronic performance of the FA-based phase pure 2D-MHPs is still lacking. MHPs in single-crystal form would be ideal for analyzing fundamental properties due to large grain boundaries, lesser defects, long diffusion length, and sustainability against high current densities.^[26–29] Therefore, the growth of homogeneous large-area 2D MHP single-crystals is pivotal for the stability analysis to explore them into a wide range of optoelectronic applications. However, synthesis and large size single-crystal growth of phase pure 2D-MHPs, particularly for higher “*n*” series, is quite challenging due to extensive organic moieties, quasi/multiphase contamination, and random stacking due to rapid nucleation. Randomly stacked 2D hybrid perovskite single-crystals with phenyl ethyl ammonium (PEA) cation grown from a supersaturated HI solution by the slow cooling method were found to exhibit ultralow self-doping concentrations.^[30]

Recently, we have demonstrated the growth of phase pure, high-quality millimeter size homologous 2D-MHPs (BA)₂(MA)_{*n*-1}Pb_{*n*}X_{3*n*+1} (*n* = 1, 2, and 3) single-crystals by slow evaporation at constant temperature (SECT) solution growth method for optical resonators.^[31,32] Herein, we used the SECT

method to grow a high-quality centimeter long (BA)₂FAPb₂I₇ single-crystal to systematically investigate degradation stability and optoelectronic properties. We found that the large area FA-based 2D hybrid perovskite single-crystal shows good stability against atmospheric degradation and laser irradiation compared to their potential counterpart of the MA-based (BA)₂MAPb₂I₇ single-crystal. Due to the enhanced stability, the (BA)₂FAPb₂I₇ single-crystal exhibits durable photodetector performance on both the rigid and the flexible polymer substrates.

2. Results and Discussion

The phase pure 2D (BA)₂(FA)Pb₂I₇ compound having two perovskite layer thicknesses (*n* = 2) was synthesized by the stoichiometric reaction of PbI₂, HC(=NH)NH₃I (FAI), and C₄H₉NH₃I (BAI) in I₂ free HI solution. H₃PO₂ was used to form an I₂-free HI solution. More details about the synthesis are given in the Experimental Section. An accurate concentration of BA is crucial in this reaction because it effectively controls reaction kinetics. The concentration of each reactant was optimized based on the earlier report by Stoumpos et al.^[10] The rectangular dark brown crystalline flakes obtained from the above reaction were used to grow high-quality single-crystals. The schematic illustration of **Figure 1a** reveals the SECT growth process. Accordingly, a saturated solution with solvent-solute equilibrium was achieved by dissolving as-synthesized (BA)₂FAPb₂I₇ flakes (Figure S1, Supporting Information) into the I₂ free HI solvent at 80 °C; it was then subjected to slow evaporation at a constant temperature. Due to solvent evaporation, the excessive solute nucleates as a tiny seed at the different positions of the beaker bottom by spontaneous nucleation. After 3 days of the growth period, well-faceted, rectangular-shaped crystals were obtained. The photo

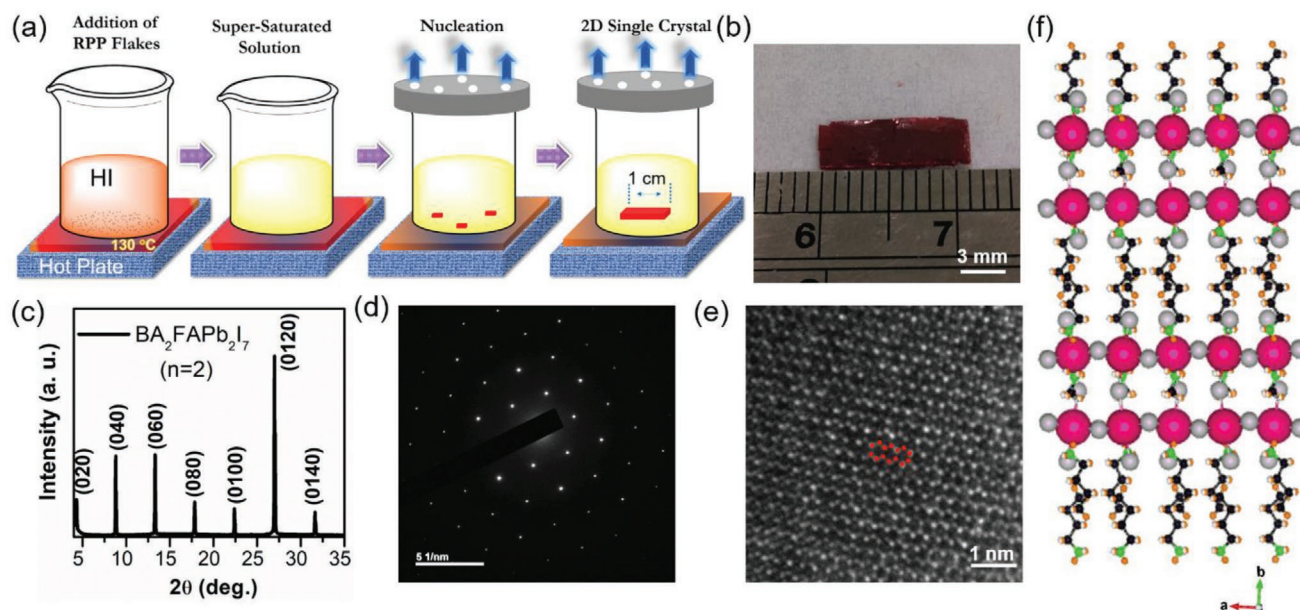


Figure 1. a) Schematic illustration of the SECT method for growing high-member 2D perovskite single-crystals. b) Photograph of as-grown centimeter long 2D (BA)₂FAPb₂I₇ perovskite single-crystal by SECT method. c) Indexed XRD pattern with repeated (0*k*0) miller planes. d) SAED pattern with linearly ordered bright diffraction spots confirms the single-crystallinity. e) A regular hexagonal arrangement of atoms was observed in the HR-TEM image, indicating a conductive perovskite layer on the top surface. f) The RP phase 2D (BA)₂FAPb₂I₇ crystal structure has two perovskite layers.

image of the as-grown centimeter-long 2D $(\text{BA})_2\text{FAPb}_2\text{I}_7$ single-crystal of dimension $1.1 \text{ cm} \times 0.4 \text{ cm}$ is shown in Figure 1b.

The phase purity and single-crystallinity of the as-grown 2D $(\text{BA})_2\text{FAPb}_2\text{I}_7$ perovskite single-crystal was examined by X-ray diffraction (XRD) and transmission electron microscopic (TEM) analysis. Figure 1c shows the XRD pattern of 2D perovskite single-crystal indexed with respect to RP phase monoclinic crystal structure. The periodic repetitions of diffraction planes in the XRD pattern indicate single-crystallinity. The characteristic features of the XRD pattern were typically used to precisely determine the number of perovskite layers (quantum well thickness) by means of the unit cell expansion in 2D perovskites. By introducing FA/or MA cation into the $(\text{BA})_2\text{PbI}_4$ ($n = 1$) crystal structure (where the thickness of one layer of perovskite is $\approx 6.41 \text{ \AA}$), the unit cell incrementally expands by the addition of each perovskite layer at a time. In the case of RP phase 2D hybrid perovskite, $n = 2$, the thickness of the perovskite increased to two layers, $\approx 12.55 \text{ \AA}$ (Figure S2b, Supporting Information). An addition of each perovskite layer expands the unit cell resulting in additional low angle reflection below $2\theta = 14^\circ$ in the XRD pattern. As shown in Figure 1c, the formation of two low angle diffraction peaks below $2\theta = 14^\circ$ in the XRD pattern reveals two perovskite layer thicknesses ($n = 2$) in the crystal structure. Based on the XRD study, the predominant crystal growth orientation of the $(\text{BA})_2\text{FAPb}_2\text{I}_7$ single-crystal was found along the b -axis. The XRD results obtained from this study are good in agreement with the standard literature report.^[10,33] The 2θ cut-off

numbering ($2\theta = 14^\circ$) is based on the fact that, at this angle, the d spacing values matches the distance between the discrete perovskite layers in both the 2D [(111) reflection $d_{111} = 6.26 \text{ \AA}$] and 3D [(110) reflection; $d_{110} = 6.26 \text{ \AA}$] perovskites.^[10,34] This numerical estimation of the crystal structure is highly recommended to study the $(\text{BA})_2(\text{MA})_{n-1}\text{Pb}_n\text{I}_{3n+1}$ and related RP hybrid perovskite compounds.^[10] For 2D hybrid perovskite with $n = 2$, the XRD shows two evenly spaced reflections (Figure S2, Supporting Information), and other high member series, such as $n = 3, 4$, and 5 , shows a corresponding number of reflections below this cut-off value $2\theta = 14^\circ$ in the XRD patterns, which in turn confirm the number of perovskite layer and phase purity.^[10,35,36]

The selective area diffraction pattern (Figure 1d) obtained from TEM analysis reveals the linearly ordered bright diffraction spots, which further confirms single-crystallinity. Moreover, the high quality of the large area single-crystal (TEM image: Figure S3, Supporting Information) allows us to record lattices with hexagonal patterns attributed to the conductive perovskite top layer by using a high-resolution TEM study (Figure 1e). The formation of a conductive perovskite top surface would be beneficial for electronic applications. Figure 1f shows the crystal structure of $(\text{BA})_2(\text{FA})\text{Pb}_2\text{I}_7$, where PbI_6 perovskites are oriented along the crystal surface. The thickness of one-layer perovskite was estimated to be 0.6 nm in hybrid 2D RP-phase architectures.

The optical homogeneity and phase purity of the 2D perovskite single-crystal was further examined by spatially correlated photoluminescence (PL) spectral studies. Figure 2a shows the

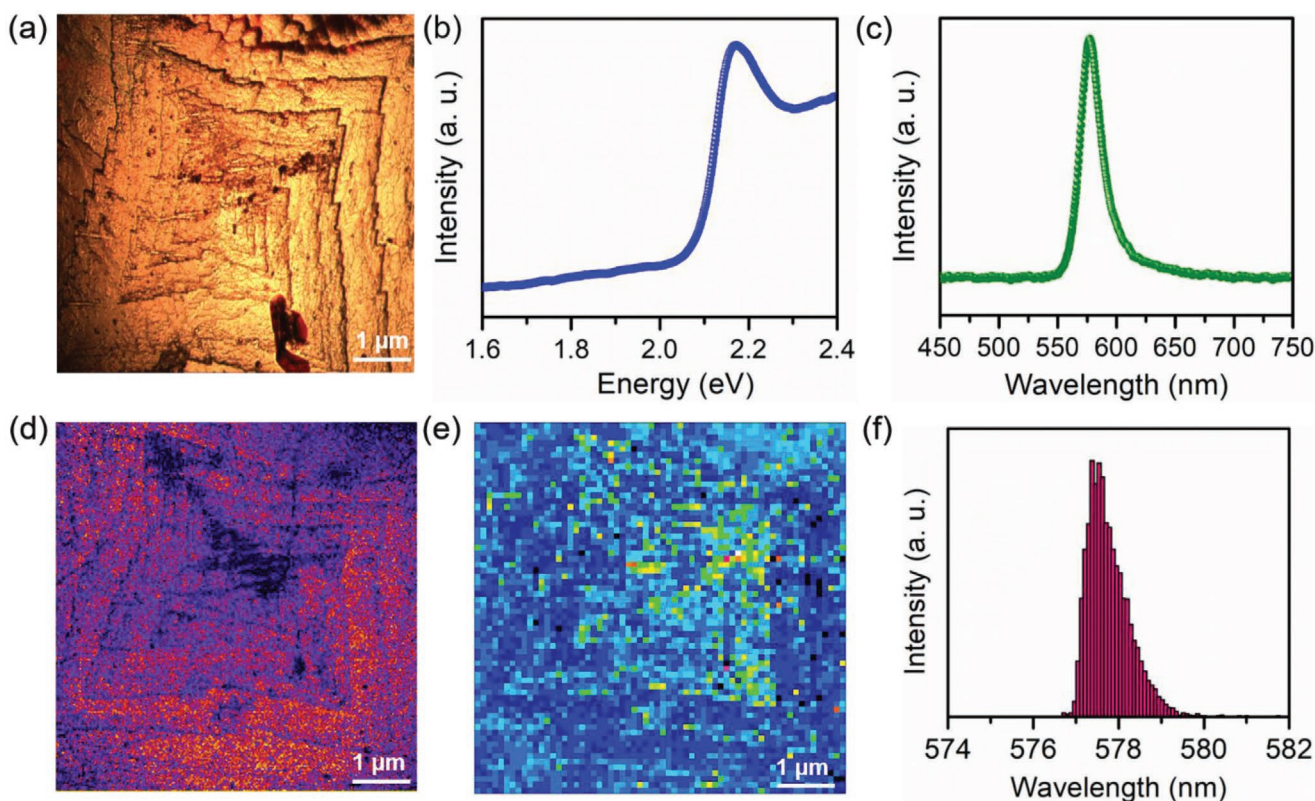


Figure 2. a) Optical image of the $(\text{BA})_2\text{FAPb}_2\text{I}_7$ single-crystal top surface. b) The optical absorption spectrum reveals a sharp absorption band at the bandgap energy of 2.17 eV . c) Photoluminescence (PL) spectrum with intense emission centered at a wavelength of 577 nm . d) The crystal top surface used for the PL spectral mapping and e) the spectral mapping image. f) The histogram of the peak wavelength measured over the top surface and the emission spectra are distributed between 576 and 581 nm , confirming the uniformity of $(\text{BA})_2\text{FAPb}_2\text{I}_7$ single-crystal.

optical microscopic image of a top surface of the $(\text{BA})_2\text{FAPb}_2\text{I}_7$ ($n = 2$) single-crystal with the dimension of about $5 \mu\text{m} \times 5 \mu\text{m}$, respectively, in which the surface morphology reveals a pyramid-like growth pattern as observed in MA-based RP phase 2D-MHPs.^[31] Figure 2b depicts the optical absorption spectrum obtained with strong narrowband absorption at the optical band gap energy of 2.17 eV, indicating the direct bandgap semiconducting behavior. Figure 2c shows the PL emission spectra measured at the excitation wavelength of 488 nm. An intense PL occurred at the wavelength of emission maxima centered at 577 nm having full-width half maxima $\approx 23 \text{ nm}$.^[37] There are no additional PL signals related to the quasi-phase contamination which reveals the phase purity of the single-crystal. The PL spectral mapping was carried out over the large area of the grown crystal to examine the PL homogeneity (Figure 2d). The spatially resolved PL spectral image was obtained with a collection of total mapping pixels of 64×64 is shown in Figure 2e. The uniform spectral distribution of emission wavelength over the entire crystal region reveals the optical homogeneity of the as-grown single-crystal. The histogram (Figure 2f) reveals the collective PL emission spectra over the entire crystal region distributed between 576 and 581 nm, indicating that the superior uniformity of the as-grown 2D perovskite crystal.

To investigate the material stability, the optical properties and surface features of the 2D $(\text{BA})_2\text{FAPb}_2\text{I}_7$ single-crystal exposed under open laboratory atmospheric conditions (relative humidity $\approx 68\%$ and room-temperature $\approx 29 \text{ }^\circ\text{C}$) were monitored using PL spectroscopy and optical microscopy at regular time intervals, 0, 30, and 60 min, respectively. The results were compared with $(\text{BA})_2\text{MAPb}_2\text{I}_7$ single-crystal counterparts under the same conditions to evaluate the relative enhancement instability. Both single-crystals were exfoliated using the standard scotch tape procedure on a silicon wafer. As shown in Figure 3a, the $(\text{BA})_2\text{FAPb}_2\text{I}_7$ crystal exhibits stable PL emission and no atmospheric degradation even after 60 min at open atmospheric exposure. At the same time, the $(\text{BA})_2\text{MAPb}_2\text{I}_7$ loose PL emission intensity half of its original value within 30 min and completely vanishes in 60 min time duration (Figure 3b).^[33,38] This phenomenon was verified with the aid of optical microscopy analysis. From the optical microscopy images, the $(\text{BA})_2\text{MAPb}_2\text{I}_7$ single-crystal starts to degrade rapidly when the time is prolonged (Figure S4, Supporting Information). 50% of the total surface degrades in 30 min of time duration and complete degradation after 60 min, which leads to a total loss of PL emission (Figure 3b). On the other hand, the $(\text{BA})_2\text{FAPb}_2\text{I}_7$ single-crystal shows extremely low degradation, even after 60 min ambient exposure.

The stability of these 2D hybrid perovskites under atmospheric exposure can be correlated to atmospheric moisture absorption. The moisture in the air could lead to material degradation due to water absorption by organic moieties in the hybrid perovskites. However, in the 2D RP phase $(\text{BA})_2(\text{FA})\text{Pb}_2\text{I}_7$ ($n = 2$) and $(\text{BA})_2(\text{MA})\text{Pb}_2\text{I}_7$ ($n = 2$) hybrid perovskites, the long-chain BA cation is a hydrophobic spacer, which is reluctant to moisture absorption. It has been widely proved that the long-chain BA spacer is crucial for enhanced environment stability in the 2D layered structure perovskites. Tsai et al. reported 2D RP phase $(\text{BA})_2(\text{MA})_3\text{Pb}_4\text{I}_{14}$ ($n = 4$) perovskite with superior long-term stability with slower degradation under

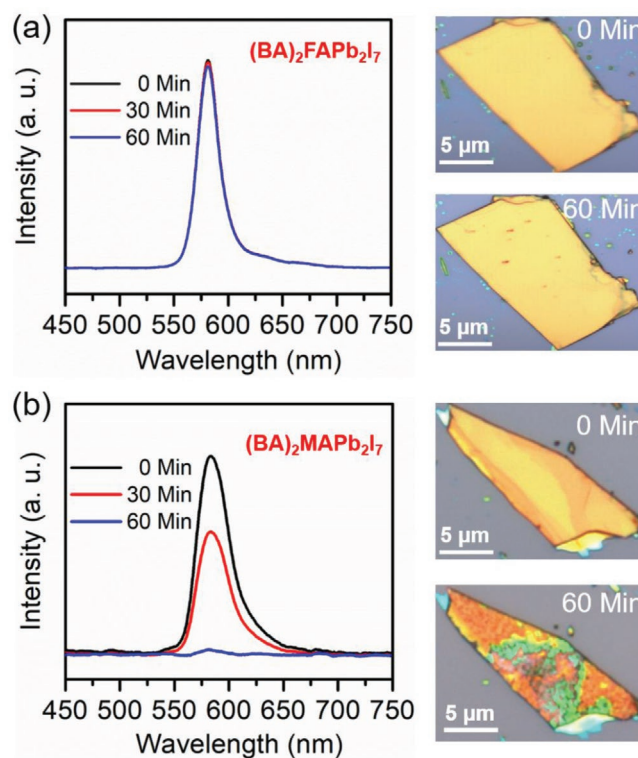


Figure 3. Optical stability of $(\text{BA})_2\text{FAPb}_2\text{I}_7$ and $(\text{BA})_2\text{MAPb}_2\text{I}_7$ single-crystals: a) The $(\text{BA})_2\text{FAPb}_2\text{I}_7$ crystal shows stable PL emission and no atmospheric degradation even after 60 min of exposure at the ambient environment. b) The $(\text{BA})_2\text{MAPb}_2\text{I}_7$, the PL emission intensity starts to diminish. Half of its intensity was lost within 30 min and completely vanishes in 60 min; this effect was clearly seen in the optical image of the right side, and the crystal degraded.

humid atmosphere as compared to the 3D MAPbI_3 , and they claimed it enhanced the stability of the $(\text{BA})_2(\text{MA})_3\text{Pb}_4\text{I}_{14}$ due to the hydrophobicity of the BA spacer.^[39] Wang et al. demonstrated ambient-air-stable solar cells formed by BA-incorporated mixed-cation (FA/Cs) perovskite. The hybrid perovskite with BA/FA/Cs showed long-term stability compared to the FA/Cs alone perovskite.^[40] In our study, atmospheric degradation in $(\text{BA})_2(\text{FA})\text{Pb}_2\text{I}_7$ ($n = 2$) and $(\text{BA})_2(\text{MA})\text{Pb}_2\text{I}_7$ ($n = 2$) might indicate the role of small MA and formamidinium (FA) cations. As an experimental fact, the $(\text{BA})_2(\text{MA})\text{Pb}_2\text{I}_7$ ($n = 2$) degrades faster than $(\text{BA})_2(\text{FA})\text{Pb}_2\text{I}_7$ ($n = 2$). The rapid degradation of $(\text{BA})_2(\text{MA})\text{Pb}_2\text{I}_7$ indicates moisture-assisted internal migration of loosely bound MA cations due to a small ionic radius and low tolerance in the perovskite lattice.^[21,22] On the other hand, the large ionic radius with the tolerance factor of FA cation leads to a stable perovskite crystal structure with enhanced atmospheric stability under the protection of BA cation.^[23]

To distinguish between $(\text{BA})_2\text{FAPb}_2\text{I}_7$ and $(\text{BA})_2\text{MAPb}_2\text{I}_7$ single-crystals, the presence of different functional groups was examined by Fourier Transform infrared spectroscopy (FT-IR) spectroscopy.^[41,42] Figure 4a shows that the FT-IR spectra were measured in the wavenumber ranges from 400 to 4000 cm^{-1} . The formation of IR bands between 3100 and 3420 cm^{-1} is assigned for the N–H stretching vibration from the primary alkyl ammonium cation. The bands observed between

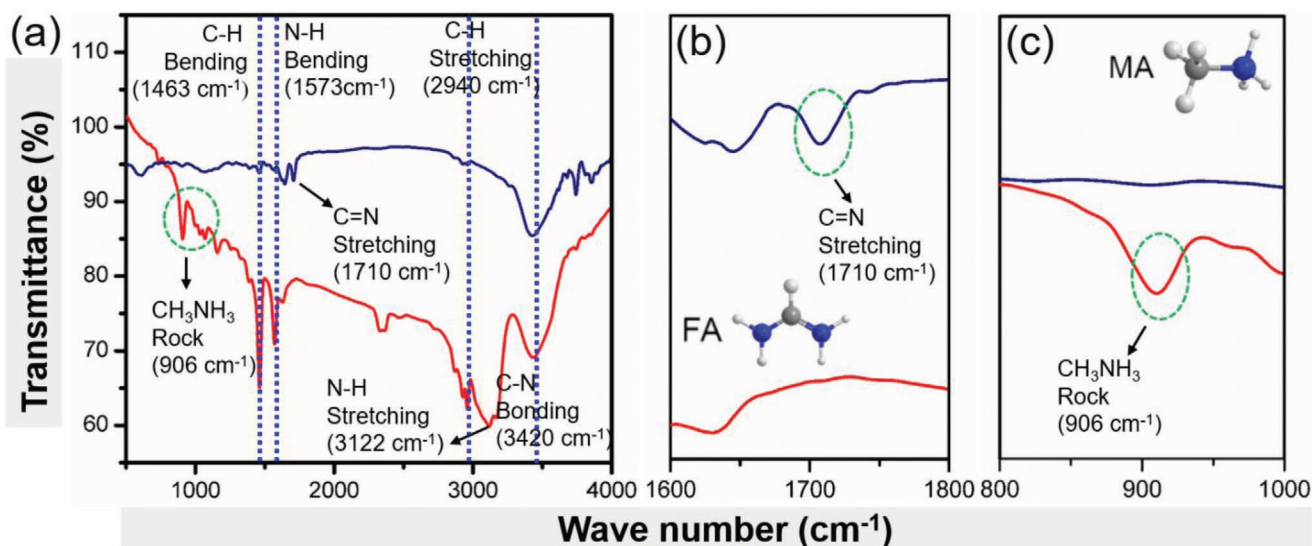


Figure 4. a) FT-IR spectra of fresh $(\text{BA})_2\text{FAPb}_2\text{I}_7$ (blue curve) and $(\text{BA})_2\text{MAPb}_2\text{I}_7$ (red curve) crystals in an open atmosphere. b,c) The formation of characteristics $-\text{C}=\text{N}$ stretching band at 1710 cm^{-1} observed for the FA is absent in MA (b) and the band at 906 cm^{-1} corresponding to CH_3NH_3 rocking is absent for FA (c).

2800 and 2950 cm^{-1} correspond to alkyl $\text{C}-\text{H}$ stretching. The sharp peaks formed at 1573 and 1463 cm^{-1} for the $(\text{BA})_2\text{MAPb}_2\text{I}_7$ are assigned for CH_3 bending vibration. The formation of a sharp band at a wavenumber 906 cm^{-1} was observed for the $(\text{BA})_2\text{MAPb}_2\text{I}_7$ assigned for the characteristic rocking vibration of $-\text{CH}_3\text{NH}_3$, which is a complete absence for the $(\text{BA})_2\text{FAPb}_2\text{I}_7$ (Figure 4b) single-crystal. On the other hand, the characteristic $-\text{C}=\text{N}$ stretching vibration at 1710 cm^{-1} is only observed for the $(\text{BA})_2\text{FAPb}_2\text{I}_7$ compound (Figure 4c).

By considering the advantage of all benefits, such as good crystallinity with a large area, strong optical absorption, and chemical/optical degradation stability, the phase pure 2D $(\text{BA})_2\text{FAPb}_2\text{I}_7$ single-crystal was used as photoactive material on both rigid and flexible optoelectronic devices. A few-layered $(\text{BA})_2\text{FAPb}_2\text{I}_7$ -field-effect transistor (FET) was fabricated by using a standard shadow mask technique. The $(\text{BA})_2\text{FAPb}_2\text{I}_7$ nanosheets were obtained by the exfoliation scotch tape process and transferred onto the silicon substrate on the top with 300 nm thick SiO_2 dielectric layers (Figure S5, Supporting Information). Then, the Cr/Au metal electrodes of thicknesses $5\text{ nm}/70\text{ nm}$ were deposited at a high vacuum using a thermal evaporation system. Figure 5a represents the schematic illustration of $(\text{BA})_2\text{FAPb}_2\text{I}_7$ -FET under 488 nm laser irradiation. The channel (perovskite) current between drain and source (I_{ds}) under bias voltage (V_{ds}) was measured, the plot of $I_{\text{ds}}-V_{\text{ds}}$ is shown in Figure 5b (Figure S6a, Supporting Information, for $(\text{BA})_2\text{MAPb}_2\text{I}_7$), in the presence and absence of light. Upon increasing illumination light intensity, the channel current was found to increase linearly. Figure 5c displays the plot of generated photocurrent (I_{ph}) as a function of the incident laser power (P), where $I_{\text{ph}} = I_{\text{light}} - I_{\text{dark}}$ was calculated by subtracting the I_{ds} obtained in the dark (represented by I_{dark}) from that under illumination (denoted by I_{light}) at $V_{\text{ds}} = 10\text{ V}$, and $V_{\text{g}} = 0\text{ V}$ (Figure S6b, Supporting Information, for $(\text{BA})_2\text{MAPb}_2\text{I}_7$). Photoresponsivity (R_{λ}) is a significant factor to critic the sensitivity of a photodetector under the light stimulus, which is defined as

the photocurrent produced per unit power of the incident light on active channel area, is expressed as $R_{\lambda} = \Delta I_{\lambda} / (P_{\lambda} S)$, where ΔI_{λ} is the generated photocurrent, P_{λ} is the incident light power, and S is the illuminated area. Figure 5d demonstrates the R_{λ} for incident laser intensity (P) values at 488 nm . The maximum R_{λ} value of $\approx 5.0\text{ A W}^{-1}$ at $3.5\text{ }\mu\text{W}$ ($V_{\text{ds}} = 10\text{ V}$ and $V_{\text{g}} = 0\text{ V}$) was obtained from $(\text{BA})_2\text{FAPb}_2\text{I}_7$ -FET. The R_{λ} value of $(\text{BA})_2\text{FAPb}_2\text{I}_7$ -FET is 25 times higher than that of the $(\text{BA})_2\text{MAPb}_2\text{I}_7$ -FET (0.2 mA W^{-1}), shown in Figure S6c, Supporting Information. Besides, the obtained responsivity of $(\text{BA})_2\text{FAPb}_2\text{I}_7$ compound is compared with reported photodetectors fabricated using other 2D and 3D hybrid perovskites (Table S1, Supporting Information).^[43–50] There are few reports on the enhanced responsivity of 2D hybrid perovskites using different strategies. Tan et al. used graphene as a protection layer and top contact for effective carrier collection in their $(\text{BA})_2\text{PbBr}_4$ photodetector to enhance the stability and responsivity.^[51] Loi et al. demonstrated high photoresponsivity by hot-casting 2D/3D vertical hetero-junction perovskite films.^[52] In this study, we showed the photodetector response of the pristine $(\text{BA})_2\text{FAPb}_2\text{I}_7$ -FET without any additional strategies. Intriguingly, the R_{λ} of $(\text{BA})_2\text{FAPb}_2\text{I}_7$ -FET increases to 63 A W^{-1} by tuning V_{bg} from 0 to $+120\text{ V}$. The plot of transfer curve (I_{ds} vs V_{bg}) under various V_{bg} from -80 to $+120\text{ V}$ is shown in Figure 5e. A solid increase in current (I_{ds}) with increasing (V_{bg}) was observed, which clearly reveals n-type semiconducting behavior, and confirms that the majority of charge carriers are electrons in the RP phase 2D $(\text{BA})_2\text{FAPb}_2\text{I}_7$ perovskite single-crystal. The n-type semiconducting behavior is consistent with the recently reported $(\text{BA})_2\text{MAPb}_2\text{I}_7$ single-crystalline FET device.^[32] The channel current was observed to increase dramatically relative to the dark state: the R_{λ} increases by simply tuning the gate voltage (V_{bg}) as shown in Figure 5f. Remarkably, the R_{λ} increased significantly from 3.8 to 63 A W^{-1} when V_{bg} was swept from 0 to $+120\text{ V}$. The obtained immense R_{λ} value can be attributed to the high-quality large-area perovskite crystal with lesser defects, stabilized crystal structure, and high

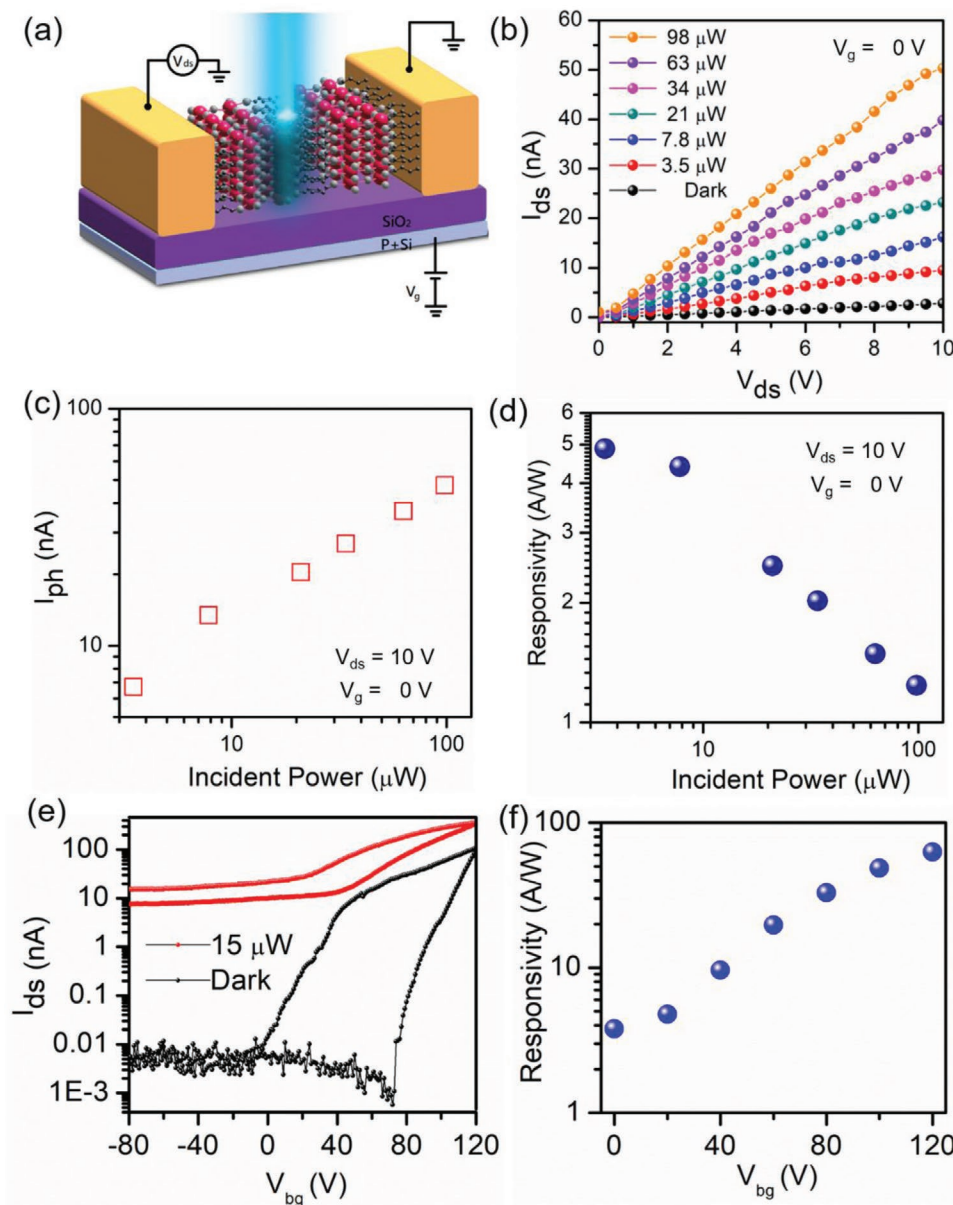


Figure 5. a) Schematic illustration of the $(\text{BA})_2\text{FAPb}_2\text{I}_7$ -FET device. b) $I_{\text{ds}}-V_{\text{ds}}$ curves in the dark and under laser ($\lambda = 488$ nm) irradiation with different intensities. c) Irradiance dependence of photocurrent of the device under 10 V bias and $V_{\text{g}} = 0$ V. d) Responsivity is a function of illumination intensity ranges from 3.5 to 98 μW of 488 nm wavelength. e) The $I_{\text{ds}}-V_{\text{bg}}$ curve with V_{bg} scanned from -80 to $+120$ V at $V_{\text{ds}} = 10$ V under light illumination and dark states. f) R_{λ} of the $(\text{BA})_2\text{FAPb}_2\text{I}_7$ photodetector as a function of V_{bg} measured at $V_{\text{ds}} = 10$ V and $P = 15$ μW .

absorption coefficient, along with the direct bandgap nature of $(\text{BA})_2\text{FAPb}_2\text{I}_7$ crystal. All the above features of FA-based 2D perovskites enable strong light absorption, efficient photocarrier generation, and the excited charge carrier's movement to the electrodes before it recombines at the channel during the light stimulus.

In addition other important photodetector parameters, such as specific detectivity (D^*) and normalized gain, were analyzed. The D^* value helps to identify the weak optical signals of a photodetector and is defined by $D^* = (S \times \Delta f)^{1/2} / \text{NEP}$, where S and Δf are the effective area and electrical bandwidth of the photodetector, respectively, and NEP

represents noise equivalent power. The NEP is a pointer to the minimum optical power that a photodetector can use to discriminate signals from noise. At low NEP value, the above equation is used simply as $D^* = R_{\lambda} S^{1/2} / (2eI_{\text{dark}})^{1/2}$, where R_{λ} , S , e , and I_{dark} are the photoresponsivity, effective area, elementary charge, and dark current, respectively.^[53] The obtained D^* value for the few-layered $(\text{BA})_2\text{FAPb}_2\text{I}_7$ is $\approx 3.5 \times 10^{11}$ Jones (at $V_{\text{g}} = 0$ and $V_{\text{ds}} = 10$ V), shown in Figure S7a, Supporting Information. The acquired D^* value for $(\text{BA})_2\text{FAPb}_2\text{I}_7$ single-crystal is approximately three orders higher than the $(\text{BA})_2\text{MAPb}_2\text{I}_7$ and approximately two times larger than the recently reported 2D-MHPs.^[54,55] Also, very

close to the commercial diodes.^[56] The normalized gain was calculated by the given relation $\Gamma_n = (E/e)(I_{ph}/p)(L^2/V)$, where E is the photon energy, e is the elementary charge, V is the bias voltage, L is the channel length of the device.^[57] From the above relation, the calculated value of Γ_n is $1.2 \times 10^{-6} \text{ V}^{-1} \text{ cm}^2$ (Figure S7b, Supporting Information), which is two orders higher compared with $(\text{BA})_2\text{MAPb}_2\text{I}_7$ -FET (Figure S8, Supporting Information).

The time-resolved (I_{ds} - t) measurements were conducted to show the photoresponse, photoswitching stability, and durability of the $(\text{BA})_2\text{FAPb}_2\text{I}_7$ photodetector at room temperature. The I_{ds} - t plot was recorded by exciting the multilayered $(\text{BA})_2\text{FAPb}_2\text{I}_7$ device with a train of ON-OFF illumination at 488 nm. Figure S9a,b, Supporting Information, shows the $(\text{BA})_2\text{FAPb}_2\text{I}_7/(\text{BA})_2\text{MAPb}_2\text{I}_7$ -FET device in response to an ON-OFF train cycle at $V_{ds} = 10 \text{ V}$ and $V_g = 0 \text{ V}$, which exhibits a fast rise of current (I_{ds}) under illumination and a quick drop followed by a much slower relaxation after switching off the laser. From the curve I_{ds} - t , the rising time of the photo-generated signal was found to be $\approx 20 \text{ ms}$. The falling time contains two components with a fast decay of $\approx 20 \text{ ms}$ (corresponding to the earlier 50% decrease) and slow relaxation of 1 s (in the later half decline). In response to consecutive photoswitching, the robustness and stability of our $(\text{BA})_2\text{FAPb}_2\text{I}_7$ single-crystal photo device was examined by a train of pulsed illumination over a long period ($\approx 1 \text{ h}$); the device shows good stability under ambient condition, as demonstrated by the I_{ds} - t measurements presented in the Figure 6a. The photoswitching measurements were conducted multiple times to demonstrate the reproducibility of long-term stability in $(\text{BA})_2\text{FAPb}_2\text{I}_7$ (Figure S10, Supporting Information). The I_{ds} - t

plot of $(\text{BA})_2\text{MAPb}_2\text{I}_7$ shown in Figure 6b, where the ON-OFF curve starts to degrade after 30 min and wholly lost signal after 60 min, is well consistent with results of optical degradation shown in Figure 3b.

We have further studied the 2D $(\text{BA})_2\text{FAPb}_2\text{I}_7$ crystal performance on a flexible photodetector using polyethylene terephthalate (PET) substrate. The $(\text{BA})_2\text{FAPb}_2\text{I}_7$ photodetector was fabricated on a PET polymer substrate by the scotch tape exfoliation procedure and followed by the Au electrode deposition as schematically illustrated in Figure 7a. As observed in $(\text{BA})_2\text{FAPb}_2\text{I}_7$ photodetector on a rigid substrate, flexible photodetector also clutches a good contact, clearly noticed in the I_{ds} - V_{ds} measurements (Figure 7b). The device channel is more conductive with a 488 nm wavelength laser illumination because of numerous photoexcited carriers in the $(\text{BA})_2\text{FAPb}_2\text{I}_7$ perovskite. The photocurrent was measured at laser illumination with different power intensities to evaluate the performance of the $(\text{BA})_2\text{FAPb}_2\text{I}_7$ single-crystal at bending and nonbending states. The photocurrent rises with increasing laser intensity, from which the photo responsivity was calculated to be 0.1 A W^{-1} , at 0.2 mW and 10 V, as shown in Figure 7c. Figure 7d shows the responsivity under different bending curvatures (1 and 2 cm). We witnessed that the responsivity value changes and reduces at bending states compared with the balanced state. The fall of responsivity in a bending state might be attributed to the induced strain in the channel, thus reducing electron-hole pair generation efficiency.^[58] In addition, the formation of the crack on the Au metal pads during the bending further reduces the responsivity values.^[59] Typically, the flaws in the metal electrode build high contact resistance with $(\text{BA})_2\text{FAPb}_2\text{I}_7$ perovskite, which additionally reduces the responsivity. Overall, the device

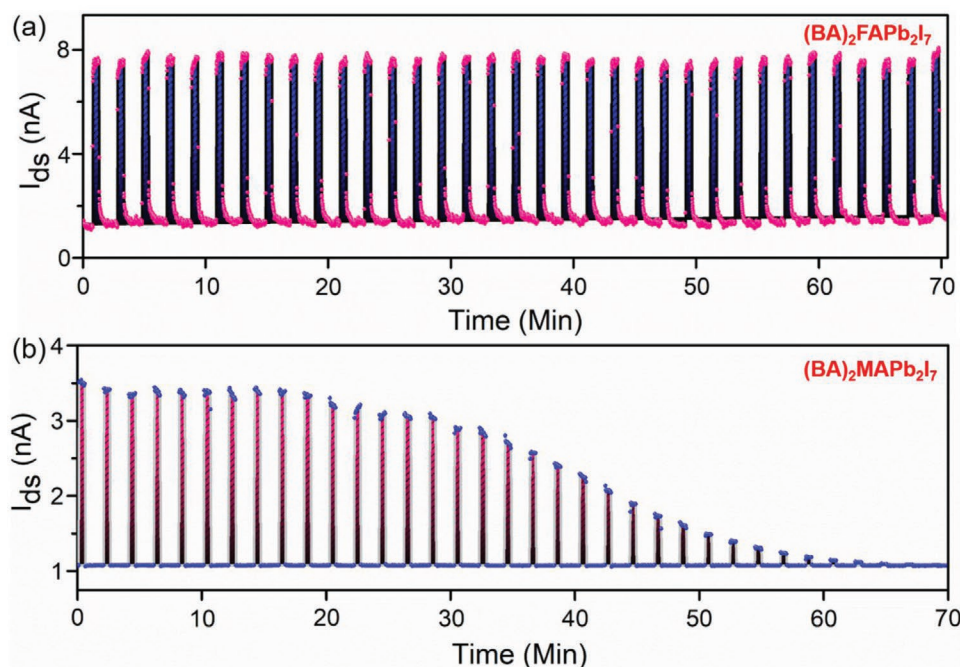


Figure 6. Photoswitching stability study for the 2D $(\text{BA})_2\text{FAPb}_2\text{I}_7/(\text{BA})_2\text{MAPb}_2\text{I}_7$ -FET device in response to a train of pulsed illumination at $\lambda = 488 \text{ nm}$, $P = 3.50 \mu\text{W}$, and $V_{ds} = 10 \text{ V}$ at ambient environment. a) The time-resolved (I_{ds} - t) measurement of $(\text{BA})_2\text{FAPb}_2\text{I}_7$ shows the strong ambient and laser stability without photocurrent degradation from its initial value at 0 to 60 min long run. b) The I_{ds} - t curve of $(\text{BA})_2\text{MAPb}_2\text{I}_7$ starts to degrade after reaching 20 min and completely vanishes at 60 min.

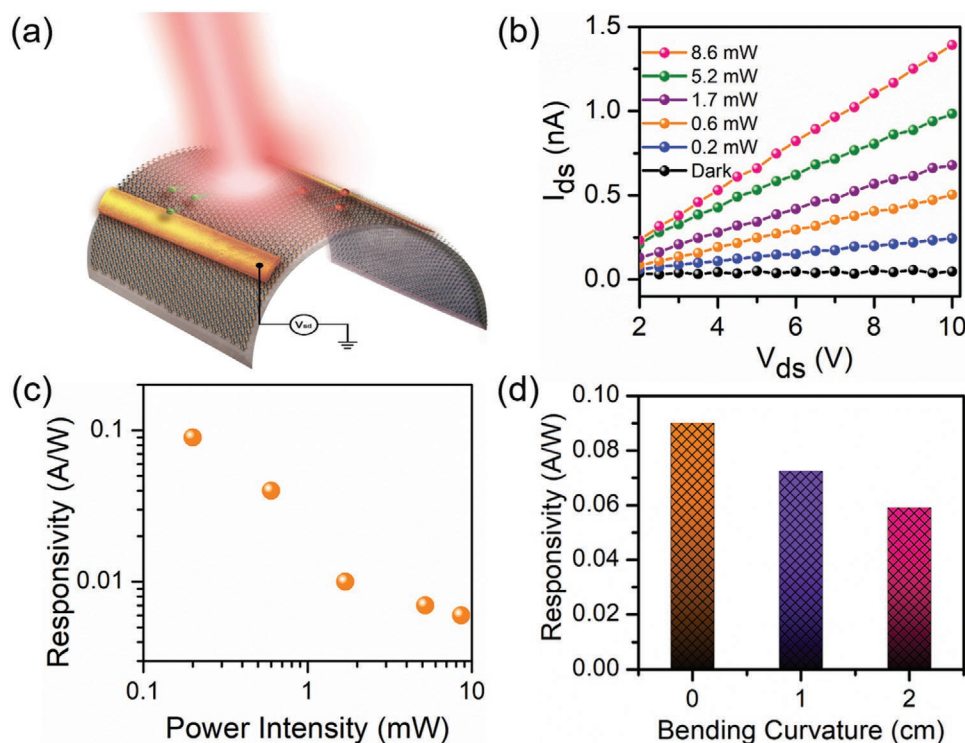


Figure 7. Optoelectronic properties of a flexible photodetector. a) Schematic illustration of a 2D $(\text{BA})_2\text{FAPb}_2\text{I}_7$ on a PET substrate. b) The I_{ds} - V_{ds} curve of the few-layered $(\text{BA})_2\text{FAPb}_2\text{I}_7$ photodetector on PET was measured in the dark and light illumination. c) The calculated responsivity as a function of the illumination intensity acquired in planar geometry at $V_{ds} = 10$ V. d) Responsivity test of the $(\text{BA})_2\text{FAPb}_2\text{I}_7$ device under bent of different radius (1 and 2 cm) and unbent state.

performance showed that 2D $(\text{BA})_2\text{FAPb}_2\text{I}_7$ can effectively work under strain-induced modulation without much deterioration. These outcomes disclose a favorable flexible nature of $(\text{BA})_2\text{FAPb}_2\text{I}_7$ perovskite semiconductors for excellent and workable practical applications.

3. Conclusion

In summary, we have successfully demonstrated a stable and durable photodetector fabricated using FA based phase-pure centimeter-long hybrid 2D $(\text{BA})_2\text{FAPb}_2\text{I}_7$ perovskite single-crystals having good crystallinity and spectral uniformity. The $(\text{BA})_2\text{FAPb}_2\text{I}_7$ single-crystal showed a tremendous enhancement in the chemical and optical degradation stability against atmospheric oxidation and continuous laser irradiation. The robustness of the stable 2D perovskite material shows high photoresponsivity and specific detectivity on both the rigid and flexible ultraviolet photodetectors, which are much higher than that of the MA-based 2D/3D counterparts and comparable to the commercialized Si photodetector. From this study, the FA-based 2D hybrid perovskite single-crystal is highly promising for future visible detectors and wearable electronics. Moreover, replacing iodide with other halides, such as chloride and bromide, would be beneficial by adding degrees of freedom in tunability for a wide range of stable and low-cost optoelectronic applications.

4. Experimental Section

Synthesis: The raw materials, PbO, 57% aqueous HI, H_3PO_2 , $\text{C}_4\text{H}_9\text{NH}_2$ (BA), $\text{CH}_3\text{NH}_3\text{Cl}$ (MACI), and $\text{HC}(\text{NH}_2)_2\text{Cl}$ (FACI) with purity (99.99%) were obtained from Aldrich chemicals. PbO (10 mmol) was added into the solution mixture of HI (76 mmol)/ H_3PO_2 (15.5 mmol) at 70 °C under constant magnetic stirring to form a dissolved bright yellow PbI_2 solution. Concurrently, the $\text{C}_4\text{H}_9\text{NH}_3\text{I}$ (BAI) was prepared by neutralizing BA with HI by continuous magnetic stirring for 2 h in an ice bath. The measured quantity of FACI (5 mmol) was dissolved into the hot PbI_2 solution, which initially led to the precipitation of FAPbI_3 that was redissolved by heating with slightly excessive solvent to form a stable, clear, bright yellow solution. Finally, a neutralized BAI (7 mmol for $n = 2$) solution was added dropwise into the clear, bright yellow solution of FAPbI_3 to form RP phase 2D $(\text{BA})_2\text{FAPb}_2\text{I}_7$. The solution was left to cool at room temperature until dark red flakes were deposited. The deposited product was filtered and dried using suction filtration under a vacuum (Figure S1, Supporting Information). For the synthesis of $(\text{BA})_2\text{MAPb}_2\text{I}_7$, the same procedure was followed with MACI instead of FACI. Accordingly, the MACI (5 mmol) was added into the PbI_2 solution to form the MAPbI_3 bright yellow solution. To the clear yellow bright solution of MAPbI_3 , the BAI (7 mmol) solution was added to form the $(\text{BA})_2\text{MAPb}_2\text{I}_7$ compound.

Single-Crystals Growth: The synthesized $(\text{BA})_2\text{FAPb}_2\text{I}_7$ flakes were used to grow centimeter-long single-crystals using the HI/ H_3PO_2 solvent medium by the SECT solution-growth method.^[31] The HI/ H_3PO_2 solution was saturated by adding 2D perovskite with magnetic stirring at a constant temperature of 80 °C in an oil bath. The beakers containing a saturated bright yellow solution were tightly covered with a paraffin sheet. The saturated solution was then allowed for controlled evaporation by making holes at the top of the paraffin sheet. Initially,

small nuclei formed at different positions at the bottom of the beaker. Then, they started to grow into large-sized single-crystals from a supersaturated solution. After 3 days, the crystals at the bottom of the beakers become thick individual platelets of centimeter-sized homologous 2D RP-phase perovskite single-crystals. The grown crystals were then gently harvested and dried at 55 °C in an oven under reduced pressure to remove the surface adsorbed solvent.

Materials Characterization: The crystal structure and phase purity of the (BA)₂FAPb₂I₇ single-crystal were studied by XRD analysis with an X'Pert PRO-PANalytical XRD using CuK α ($\lambda = 1.5406 \text{ \AA}$) source, step size 0.01°, scan speed 0.5 s/step, and operation voltage 40 kV. The microstructural features of the grown crystal were examined by TEM using JEOL, JEM-2100F operated at 200 kV. A home-built setup was used for the photoluminescence spectral mapping with a 450 nm pulse laser (Pico Quant) as an excitation light source. The optical absorption spectra were recorded using Jacobs V-670 UV-vis spectrometer. The FT-IR was analyzed by Perkin Elmer model spectrum in the transmittance mode in the wavenumber range 400–4000 cm⁻¹.

Mechanical Exfoliation-Few layered: As-grown 2D (BA)₂FAPb₂I₇ and (BA)₂MAPb₂I₇ perovskite single-crystals were used to obtain few-layered nanosheets using a scotch tape mechanical exfoliation technique. Briefly, the bulk 2D perovskite single-crystals were gently rubbed and sliced multiple times on the top of the scotch tape to obtain a few-layered nanosheet and transferred to the Si wafer containing a 300 nm thick SiO₂ dielectric layer and PET substrates. The transferred perovskite layers were examined with an optical microscope (Olympus, BX 51M) equipped with a charge-coupled device (CCD) camera (Leica, DFC495).

Field-Effect Transistor-Device Fabrication and Optoelectronic Properties: The TEM copper grid was used to pattern the electrode on the few-layered (BA)₂FAPb₂I₇ and (BA)₂MAPb₂I₇ nanosheets with the aid of a micromanipulator. Also, the TEM grid was used as a shadow mask for the deposition of source and drain electrodes of Cr (5 nm)/Au (70 nm) using a thermal evaporation unit. The optoelectronic properties of the (BA)₂FAPb₂I₇ and (BA)₂MAPb₂I₇-FETs were studied using a probe station (Lakeshore, TTPX) equipped with a source electrometer (Keithley, 2636A) and an optical system, including a He-Ne laser (JDS Uniphase, Novette 1507), a power meter (Ophir, Nova II), and an optical beam shutter (Thorlabs, SH1).

Supporting Information

Supporting Information is available from the Wiley Online Library or from the author.

Acknowledgements

R.S. acknowledges the financial support provide by the Ministry of Science and Technology (MOST), Taiwan, under grant numbers MOST-110-2112-M-001-065-MY3 and Academia Sinica for the budget of AS-iMATE-19-110. C.-Y.L. acknowledges MOST-110-2221-E-033-022, MOST-109-2222-E-003-001-MY2. R.C.M. and A.R. acknowledge the support of Marie Skłodowska-Curie Individual Fellowship (MOFUS, #795356).

Conflict of Interest

The authors declare no conflict of interest.

Data Availability Statement

The data that support the findings of this study are available from the corresponding authors upon reasonable request.

Keywords

ambient stability, flexible electronics, photoresponsivity, specific detectivity, two-dimensional perovskites

Received: December 1, 2021

Published online:

- [1] J. Y. Kim, J.-W. Lee, H. S. Jung, H. J. Shin, N.-G. Park, *Chem. Rev.* **2020**, *120*, 7867.
- [2] L. Chouhan, S. Ghimire, C. Subrahmanyam, T. Miyasaka, V. Biju, *Chem. Soc. Rev.* **2020**, *49*, 2869.
- [3] S. D. Stranks, H. J. Snaith, *Nat. Nanotechnol.* **2015**, *10*, 391.
- [4] A. Miyata, A. Mitioglu, P. Plochocka, O. Portugall, J. T.-W. Wang, S. D. Stranks, H. J. Snaith, R. J. Nicholas, *Nat. Phys.* **2015**, *11*, 582.
- [5] Q. Dong, Y. Fang, Y. Shao, P. Mulligan, J. Qiu, L. Cao, J. Huang, *Science* **2015**, *347*, 967.
- [6] L. Dou, Y. Yang, J. You, Z. Hong, W.-H. Chang, G. Li, Y. Yang, *Nat. Commun.* **2014**, *5*, 5404.
- [7] M. A. Green, A. Ho-Baillie, H. J. Snaith, *Nat. Photonics* **2014**, *8*, 506.
- [8] Y.-H. Kim, H. Cho, J. H. Heo, T.-S. Kim, N. S. Myoung, C.-L. Lee, S. H. Im, T.-W. Lee, *Adv. Mater.* **2015**, *27*, 1248.
- [9] P. Liu, X. He, J. Ren, Q. Liao, J. Yao, H. Fu, *ACS Nano* **2017**, *11*, 5766.
- [10] C. C. Stoumpos, D. H. Cao, D. J. Clark, J. Young, J. M. Rondinelli, J. I. Jang, J. T. Hupp, M. G. Kanatzidis, *Chem. Mater.* **2016**, *28*, 2852.
- [11] H. Tsai, W. Nie, J.-C. Blancon, C. C. Stoumpos, R. Asadpour, B. Harutyunyan, A. J. Neukirch, R. Verduzco, J. J. Crochet, S. Tretiak, L. Pedesseau, J. Even, M. A. Alam, G. Gupta, J. Lou, P. M. Ajayan, M. J. Bedzyk, M. G. Kanatzidis, A. D. Mohite, *Nature* **2016**, *536*, 312.
- [12] I. C. Smith, E. T. Hoke, D. Solis-Ibarra, M. D. McGehee, H. I. Karunadasa, *Angew. Chem.* **2014**, *126*, 11414.
- [13] D. H. Cao, C. C. Stoumpos, O. K. Farha, J. T. Hupp, M. G. Kanatzidis, *J. Am. Chem. Soc.* **2015**, *137*, 7843.
- [14] H. Lai, D. Lu, Z. Xu, N. Zheng, Z. Xie, Y. Liu, *Adv. Mater.* **2020**, *32*, 2001470.
- [15] H.-P. Wang, S. Li, X. Liu, Z. Shi, X. Fang, J. H. He, *Adv. Mater.* **2021**, *33*, 2003309.
- [16] L. Zhang, C. Sun, T. He, Y. Jiang, J. Wei, Y. Huang, M. Yuan, *Light: Sci. Appl.* **2021**, *10*, 61.
- [17] Z. Ren, J. Yu, Z. Qin, J. Wang, J. Sun, C. C. S. Chan, S. Ding, K. Wang, R. Chen, K. S. Wong, X. Lu, W.-J. Yin, W. C. H. Choy, *Adv. Mater.* **2021**, *33*, 2005570.
- [18] C. Qin, A. S. D. Sandanayaka, C. Zhao, T. Matsushima, D. Zhang, T. Fujihara, C. Adachi, *Nature* **2020**, *585*, 53.
- [19] Z. Liu, M. Hu, J. Du, T. Shi, Z. Wang, Z. Zhang, Z. Hu, Z. Zhan, K. Chen, W. Liu, J. Tang, H. Zhang, Y. Leng, R. Li, *ACS Nano* **2021**, *15*, 6900.
- [20] F. Liu, L. Wang, J. Wang, F. Wang, Y. Chen, S. Zhang, H. Sun, J. Liu, G. Wang, Y. Hu, C. Jiang, *Adv. Funct. Mater.* **2021**, *31*, 2005662.
- [21] B. Conings, J. Drijkoningen, N. Gauquelin, A. Babayigit, J. D. Haen, L. D. Ollieslaeger, A. Ethirajan, J. Verbeeck, J. Manca, E. Mosconi, F. D. Angelis, H.-G. Boyen, *Adv. Energy Mater.* **2015**, *5*, 1500477.
- [22] A. Senocrate, G. Y. Kim, M. Gratzel, J. Maier, *ACS Energy Lett.* **2019**, *4*, 2859.
- [23] Q. Han, S.-H. Bae, P. Sun, Y.-T. Hsieh, Y. Yang, Y. S. Rim, H. Zhao, Q. Chen, W. Shi, G. Li, Y. Yang, *Adv. Mater.* **2016**, *28*, 2253.
- [24] J. Jeong, M. Kim, J. Seo, H. Lu, P. Ahlawat, A. Mishra, Y. Yang, M. A. Hope, F. T. Eickemeyer, M. Kim, Y. J. Yoon, I. W. Choi, B. P. Darwich, S. J. Choi, Y. Jo, J. H. Lee, B. Walker, S. M. Zakeeruddin, L. Emsley, U. Rothlisberger, A. Hagfeldt, D. S. Kim, M. Gratzel, J. Y. Kim, *Nature* **2021**, *592*, 381.
- [25] Y. Chen, M. He, J. Peng, Y. Sun, Z. Liang, *Adv. Sci.* **2016**, *3*, 1500392.

- [26] T. Liu, J. Zhang, M. Qin, X. Wu, F. Li, X. Lu, Z. Zhu, A. K.-Y. Jen, *Adv. Funct. Mater.* **2021**, *31*, 2009515.
- [27] Y. Liu, H. Xiao, W. A. Goddard III, *Nano Lett.* **2016**, *16*, 3335.
- [28] E. Penzo, A. Loiodice, E. S. Barnard, N. J. Borys, M. J. Jurow, M. Lorenzon, I. Rajzbaum, E. K. Wong, Y. Liu, A. M. Schwartzberg, S. Cabrini, S. Whitelam, R. Buonsanti, A. W. Bargioni, *ACS Nano* **2020**, *14*, 6999.
- [29] J. Wang, J. Li, S. Lan, C. Fang, H. Shen, Q. Xiong, D. Li, *ACS Nano* **2019**, *13*, 5473.
- [30] W. Peng, J. Yin, K.-T. Ho, O. Ouellette, M. D. Bastiani, B. Murali, O. E. Tall, C. Shen, X. Miao, J. Pan, E. Alarousu, J.-H. He, B. S. Ooi, O. F. Mohammed, E. Sargent, O. M. Bakr, *Nano Lett.* **2017**, *17*, 4759.
- [31] C. M. Raghavan, T.-P. Chen, S.-S. Li, W.-L. Chen, C.-Y. Lo, Y.-M. Liao, G. Haider, C.-C. Lin, C.-C. Chen, R. Sankar, Y.-M. Chang, F.-C. Chou, C.-W. Chen, *Nano Lett.* **2018**, *18*, 3221.
- [32] M.-K. Li, T.-P. Chen, Y.-F. Lin, C. M. Raghavan, W.-L. Chen, S.-H. Yang, R. Sankar, C.-W. Luo, Y.-M. Chang, C.-W. Chen, *Small* **2018**, *14*, 1803763.
- [33] E. Shi, S. Deng, B. Yuan, Y. Gao, L. Akriti, C. S. Yuan, D. Davis, Y. Zemlyanov, L. Yu, L. Huang, L. Dou, *ACS Nano* **2019**, *13*, 1635.
- [34] D. H. Cao, C. C. Stoumpos, O. K. Farha, J. T. Hupp, M. G. Kanatzidis, *J. Am. Chem. Soc.* **2015**, *137*, 7843.
- [35] D. T. Gangadharan, D. Ma, *Energy Environ. Sci.* **2019**, *12*, 2860.
- [36] J.-C. Blancon, H. Tsai, W. Nie, C. C. Stoumpos, L. Pedesseau, C. Katan, M. Kepenekian, C. M. M. Soe, K. Appavoo, M. Y. Sfeir, S. Tretiak, P. M. Ajayan, M. G. Kanatzidis, J. Even, J. J. Crochet, A. D. Mohite, *Science* **2017**, *355*, 1288.
- [37] J. Yan, W. Fu, X. Zhang, J. Chen, W. Yang, W. Qiu, G. Wu, F. Liu, P. Heremans, H. Chen, *Mater. Chem. Front.* **2018**, *2*, 121.
- [38] F. Wang, J. Ma, F. Xie, L. Li, J. Chen, J. Fan, N. Zhao, *Adv. Funct. Mater.* **2016**, *26*, 3417.
- [39] H. Tsai, W. Nie, J.-C. Blancon, C. C. Stoumpos, R. Asadpour, B. Harutyunyan, A. J. Neukirch, R. Verduzco, J. J. Crochet, S. Tretiak, L. Pedesseau, J. Even, M. A. Alam, G. Gupta, J. Lou, P. M. Ajayan, M. J. Bedzyk, M. G. Kanatzidis, A. D. Mohite, *Nature* **2016**, *536*, 312.
- [40] Z. Wang, Q. Lin, F. P. Chmiel, N. Sakai, L. M. Herz, H. J. Snaith, *Nat. Energy* **2017**, *2*, 17135.
- [41] Z. Zhou, S. Pang, F. Ji, B. Zhang, G. Cui, *Chem. Commun.* **2016**, *52*, 3828.
- [42] K. Hills-Kimball, Y. Nagaoka, C. Cao, E. Chaykovsky, O. Chen, *J. Mater. Chem. C* **2017**, *5*, 5680.
- [43] R. Dong, C. Lan, X. Xu, X. Liang, X. Hu, D. Li, Z. Zhou, L. Shu, S. Yip, C. Li, S.-W. Tsang, J. C. Ho, *ACS Appl. Mater. Interfaces* **2018**, *10*, 19019.
- [44] J. Chen, Y. Wang, L. Gan, Y. He, H. Li, T. Zhai, *Angew. Chem., Int. Ed.* **2017**, *56*, 14893.
- [45] L. Min, W. Tian, F. Cao, J. Guo, L. Li, *Adv. Mater.* **2021**, *33*, 2101714.
- [46] R. Saraf, V. Maheshwari, *ACS Appl. Mater. Interfaces* **2018**, *10*, 21066.
- [47] S. Ma, G. Jang, S. Kim, H.-C. Kwon, S. Goh, H. Ban, J. H. Cho, J. Moon, *ACS Appl. Mater. Interfaces* **2020**, *12*, 41674.
- [48] Z. Chen, Z. Kang, C. Rao, Y. Cheng, N. Liu, Z. Zhang, L. Li, Y. Gao, *Adv. Electron. Mater.* **2019**, *5*, 1900168.
- [49] Z.-X. Zhang, L.-H. Zeng, X.-W. Tong, Y. Gao, C. Xie, Y. H. Tsang, L.-B. Luo, Y.-C. Wu, *J. Phys. Chem. Lett.* **2018**, *9*, 1185.
- [50] J. Li, S. Yuan, G. Tang, G. Li, D. Liu, J. Li, X. Hu, Y. Liu, J. Li, Z. Yang, S. F. Liu, Z. Liu, F. Gao, F. Yan, *ACS Appl. Mater. Interfaces* **2017**, *9*, 42779.
- [51] Z. Tan, Y. Wu, H. Hong, J. Yin, J. Zhang, L. Lin, M. Wang, X. Sun, L. Sun, Y. Huang, K. Liu, Z. Liu, H. Peng, *J. Am. Chem. Soc.* **2016**, *138*, 16612.
- [52] H.-L. Loi, J. Cao, X. Guo, C.-K. Liu, N. Wang, J. Song, G. Tang, Y. Zhu, F. Yan, *Adv. Sci.* **2020**, *7*, 2000776.
- [53] R. K. Ulaganathan, R. Sankar, C.-Y. Lin, R. C. Murugesan, K. Tang, F.-C. Chou, *Adv. Electron. Mater.* **2020**, *6*, 1900794.
- [54] L. Qian, Y. Sun, M. Sun, Z. Fang, L. Li, D. Xie, C. Li, L. Ding, *J. Mater. Chem. C* **2019**, *7*, 5353.
- [55] Z. Li, H. Li, K. Jiang, D. Ding, J. Li, C. Ma, S. Jiang, Y. Wang, T. D. Anthopoulos, Y. Shi, *ACS Appl. Mater. Interfaces* **2019**, *11*, 40204.
- [56] X. Gong, M. Tong, Y. Xia, W. Cai, J. S. Moon, Y. Cao, G. Yu, C.-L. Shieh, B. Nilsson, A. J. Heeger, *Science* **2009**, *325*, 1665.
- [57] C.-Y. Lin, R. K. Ulaganathan, R. Sankar, R. C. Murugesan, A. Subramanian, A. Rozhin, S. Firdoz, *J. Mater. Chem. C* **2021**, *9*, 10478.
- [58] H. J. Conley, B. Wang, J. I. Ziegler, R. F. Haglund, S. T. Pantelides, K. I. Bolotin, *Nano Lett.* **2013**, *13*, 3626.
- [59] G.-H. Lee, Y.-J. Yu, X. Cui, N. Petrone, C.-H. Lee, M. S. Choi, D.-Y. Lee, C. Lee, W. J. Yoo, K. Watanabe, T. Taniguchi, C. Nuckolls, P. Kim, J. Hone, *ACS Nano* **2013**, *7*, 7931.